



Full length article

Phase-transformation assisted twinning in Molybdenum nanowires



Afnan Mostafa ^{a,1}, Linh Vu ^{a,1}, Zheming Guo ^a, Ali K. Shargh ^a, Aditya Dey ^a, Hesam Askari ^{a,b}, Niaz Abdolrahim ^{a,b,c,*}

^a Department of Mechanical Engineering, University of Rochester, Rochester, 14627, NY, USA

^b Materials Science program, University of Rochester, Rochester, 14627, NY, USA

^c Laboratory for Laser Energetics, University of Rochester, Rochester, 14627, NY, USA

ARTICLE INFO

Keywords:

Phase transformation
Twinning
Molybdenum

ABSTRACT

Systematic molecular dynamics simulations were conducted to investigate deformation mechanisms in molybdenum (Mo) nanowires (NWs) under uniaxial tensile and compressive loading, and their correlations with bulk materials containing crack tips. Our study revealed striking, orientation-dependent phase transformation and slip/twinning mechanisms. Specifically, $\langle 100 \rangle$ -loaded structures exhibited a unique $bcc_1-fcc-bcc_2$ phase transition with twin boundary formation, while $\langle 110 \rangle$ -loaded structures showed phase transformation under compression but not tension. $\langle 111 \rangle$ -loaded structures displayed no phase transformation-assisted twinning, deforming solely by slip. Bulk structures with cracks exhibited similar behavior, underscoring the high stresses needed to activate phase transformations. Density Functional Theory (DFT) calculations confirmed the metastability of the fcc phase, critical for twin formation and bcc phase reorientation. These findings highlight the potential for designing stronger, more ductile Mo-based nanomaterials, opening new avenues for advanced applications in nanotechnology and materials science.

1. Introduction

Body-centered-cubic (bcc) metals are highly desirable for use in nuclear or fusion reactors, semiconductor devices, and nanotechnologies [1–5]. Understanding the deformation mechanisms of bcc metals is crucial for improving their strength and performance. Dislocation slip and deformation twinning have been known as the most common deformation mechanisms in metals [6]. Previous experimental studies have shown that twinning is less frequently observed in bcc metals due to a higher energy barrier [7], and hence, dislocation slip remains the dominant deformation mechanism [8–12]. However, twinning opens up numerous opportunities to design nanomaterials with superior ductility without compromising much of their strength [13], otherwise known as the strength-ductility trade off [14]. Interestingly, twinning is more prone to be observed in nanoscale structures such as nanowires (NWs) or thin ligaments [15–17]. This is due to their high surface-to-volume ratio, which provides sufficient surface energy to initiate twinning formation. Despite limited experimental evidence of twinning in Mo NWs, unlike in other bcc NWs, such as W and Nb [18–20], twins can occur in nanoscale structures and have potentials to significantly enhance the deformability of Mo-based structures [21–25].

Previous studies reported that phase transformation can act as a potential stress-induced twin-formation route in alloys and metals

[26–29]. Wang et al. [30] captured two sequential localized structural transitions— bcc_1-fcc and $fcc-bcc_2$ —in pre-cracked Mo, both experimentally and computationally; they reported that high-stresses near the crack tip facilitate such local structural transitions. Lu et al. [31] showed a small-scale $bcc-fcc$ transformation in single crystal Mo NW using *in situ* tensile experiments inside a transmission electron microscope (TEM). In another study, using a high-resolution transmission electron microscope (HRTEM), Lu et al. [32] demonstrated a strain-induced $bcc-fco$ (face-centered-orthorhombic) transition at the high-stress concentration regions in Mo. These experimental studies [30–32] reported localized (*i.e.*, near the crack tip) phase transformations resulting from the high-stress concentrations. However, for enhanced ductility, it is necessary to achieve uniform and global phase transitions via nucleation and propagation of twins.

Molecular dynamics (MD) simulations are known to produce accurate results at the atomic level [33–40], including phase transformation-assisted twinning [27,29], phase transformation during deposition [41], dynamic compression [42], and phase transformation and twin formation in Mo and Cu during nanoindentation of multi-layered Cu/Mo films [43]. In their study of a simulated bi-continuous intertwined Cu-Mo composite bulk structure, where multiple inter-connected ligaments

* Corresponding author at: Department of Mechanical Engineering, University of Rochester, Rochester, 14627, NY, USA.
E-mail address: niaz@rochester.edu (N. Abdolrahim).

¹ Afnan Mostafa and Linh Vu equally contributed to this work.

of Cu and Mo led to ductile deformation, He and Abdolrahim [27] observed a uniform homogeneous bcc-fcc-bcc phase transformation utilizing the EAM potential developed by Gong et al. [44]; they showed that the presence of uniformly-distributed high-stress areas is required for achieving global phase transformations across the whole system. Wang et al. [45] previously demonstrated, employing MAEAM potential [46], a uniform and stable transformation of bcc to fcc phase in pure, pristine Mo NW through MD simulations. However, our first principle calculations, as presented in this paper, reveal that fcc represents a transient phase, serving primarily as a precursor to twin formation. Moreover, experimental evidence further supports the notion of localized and transient fcc phase emergence particularly evident at crack tips [30–32]. In another study, Wang et al. [47] observed twin formation during the tensile deformation of ⟨100⟩-loaded Mo NWs, described by Ackland-Thetford EAM potential [48]. However, this study did not investigate the mechanisms and the role of phase transformations in the nucleation of twins. Understanding this intermediate stage (*i.e.*, phase-transformation) is a crucial step towards enhancing deformability through twinning. This underscores the need to identify phase transition and twinning mechanisms in Mo NWs using systematic MD simulations. Additionally, the significance of phase transformations in initiating twin nucleation under both tensile and compressive loading conditions in Mo NWs has not been comprehensively addressed before. Hence, this research aims to provide a comprehensive understanding of the effects of the orientation on deformation mechanisms (*e.g.*, twins or slips) in Mo NWs and bulk structures with cracks under uniaxial loading conditions.

2. Methods

This research utilizes the LAMMPS [49] code to perform molecular dynamics (MD) simulations of the uniaxial tensile loading on Mo NWs and bulk structures and uniaxial compressive loading on Mo NWs. The simulations aim to investigate the orientation-dependent behavior of three different loading directions of NWs—⟨100⟩, ⟨110⟩, and ⟨111⟩. In addition, the size effect for the observed behavior will be investigated by modeling bulk structures with an elliptical crack. Table 1 defines four NW cases and two bulk cases accordingly. Fig. 1a-b and 1c show a representative Mo NW and a bulk structure with an elliptical crack, respectively. Atoms in frames 1b and 1c are colored according to their local lattice structure; that is, bcc and surface atoms are colored in blue and white, respectively. All Mo NWs in this study have a rectangular cross-section and dimensions of 3 nm × 3 nm × 19 nm. Periodic boundary conditions were imposed at both ends (*z*-axis) and non-periodic, shrink-wrapped conditions on the transverse directions (*x* and *y* axes). Although the NWs exhibit symmetrical and homogeneous characteristics, the initiation point of phase transformation is not exactly in the middle of the structure. Instead, the initiation point depends on local atomic velocities. To investigate the size effects on the phase transformation-based deformation behavior, simulations of bulk-sized structures are also conducted using a size of 58.5 nm × 8.8 nm × 37.1 nm with full periodic boundary conditions. Previous experimental work by Wang et al. [30] has shown that a local bcc-fcc-bcc was observed in a small region close to a uniaxially-loaded crack in an otherwise bulk Mo structure due to the presence of large stress concentrations at the crack tip. To reproduce the observed local phase transformation, a crack configuration is created in the bulk simulations by removing 0.1% of the atoms in an elliptical region at the center of the *x*-*y* plane and throughout the *z* direction of the structure, as shown in Fig. 1c.

Interactions between Mo atoms are described using the embedded atom method (EAM) potential developed by Gong et al. where *ab initio* calculations successfully predicted the fundamental parameters (*e.g.*, lattice constants, cohesive energies, and elastic properties) of metastable Cu-Mo and pure (Cu, Mo) phases [44]. All the structures

Table 1

Crystallographic orientations in *x*, *y*, and *z* directions of NWs and bulk structures.

Configuration	<i>x</i>	<i>y</i>	<i>z</i>
Case 1 NW	[100]	[010]	[001] - loading
Case 1 bulk	[010]	[001] - loading	[100]
Case 2 NW	[110]	[̄10]	[001] - loading
Case 2 bulk	[̄10]	[001] - loading	[110]
Case 3 NW	[11̄2]	[111]	[1̄10] - loading
Case 4 NW	[110]	[11̄2]	[111] - loading

are initially relaxed using the conjugate gradient algorithm with energy and force stopping tolerances of 10^{-26} [eV/eV] and [eV/Å], respectively. Next, these structures are equilibrated under the Nosé-Hoover isothermal-isobaric (NPT) ensemble at constant temperature (300 K) and no external pressure. After equilibration, the structures are subjected to uniaxial loading in the canonical NVT (for NWs) and NPT (for bulk) ensembles at an effective strain rate of 10^9 s⁻¹.

To visualize structural responses to uniaxial deformation, OVITO [50] is utilized. The adaptive common neighbor analysis (a-CNA) [51] algorithm is used to recognize phase transitions. Furthermore, polyhedral template matching (PTM) [52] algorithm is employed to display the lattice orientation of each phase in quaternion form [*x* *y* *z* *w*], which is then transformed into Miller indices [*h* *k* *l*] [53]. The structures are color-coded according to each phase's structure type and orientation, as shown in Fig. 3. To substantiate the validity of the observed phase transformations in OVITO, potential energy curves computed by MD and Density Functional Theory (DFT) codes are also generated as additional evidence. For the DFT method, the periodic crystal structures of each phase for all the cases obtained from MD simulations were modeled using ATOMISTIX TOOLKIT software [54,55]. First-principles simulations were performed to obtain the total energy curve of each structure with respect to the applied loading direction, using the Quantum ESPRESSO (QE) open-source DFT package [56,57]. The Perdew-Burke-Ernzerhof (PBE) form and generalized gradient approximation (GGA) have been used to treat the exchange-correlation effects [58]. The electron-ion interactions for Mo atoms are described by the ultrasoft pseudopotentials provided by QE [59,60]. A plane wave basis set with an energy cutoff of 50 Ry and a charge density threshold of 450 Ry has been considered for the simulations. The convergence criterion for solving the self-consistent equation was set to 10^{-11} Ry. Integration over reciprocal space Brillouin zone was done by using a $16 \times 16 \times 16$ k-point grid within Monkhorst-Pack [61,62]. Initially, the ground state periodic lattice constants were obtained from MD-simulated structures, which were further minimized using DFT. The structures were considered relaxed until all the atomic forces were less than 0.01 eV/Å. By calculating energies as a function of the out-of-plane lattice constant, the energy curve for each phase was obtained. The intersection of energy curves is then used to identify the phase with the lowest energy configuration and detection of the phase transformation.

3. Results & discussion

3.1. Stress-strain curves of all NWs

Figs. 2a and 2b represent stress-strain responses of all four NWs under uniaxial tension and compression, respectively, where the applied uniaxial strain (*ε*) is expressed as, $\epsilon = |\frac{l-l_0}{l_0}|$, where *l* and *l*₀ are the respective lattice constants of strained and initial Mo phases. The stress-strain curves reveal a significant difference in the deformation mechanism between cases 1–2 and 3–4 NWs under tension and between cases 1–3 and 4 under compression. Firstly, the tensile yield strength, shown in Fig. 2a, of cases 1 and 2 is ~10 GPa, whereas that of cases 3 and 4 is significantly higher, measuring at ~20 GPa and ~30 GPa, respectively. Also, Mo NWs with a loading direction of ⟨100⟩, shown by

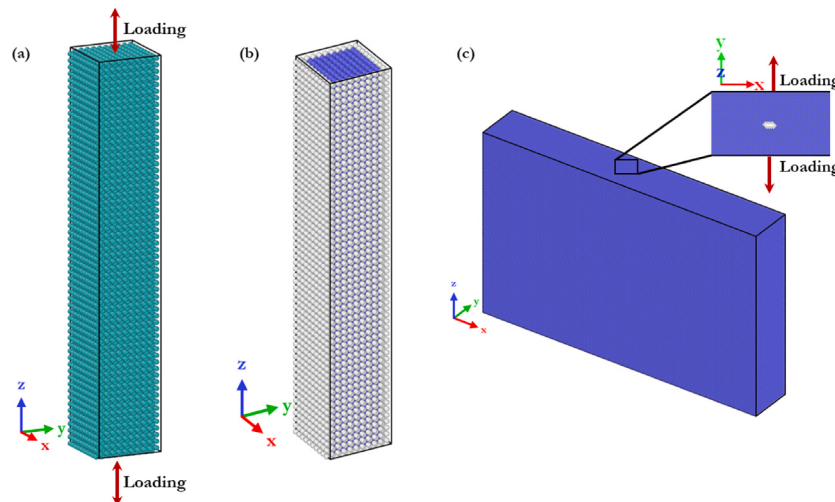


Fig. 1. A sample configuration of $\langle 100 \rangle$ -oriented Mo nanowire (NW): (a) as-generated and (b) color-coded by polyhedral template matching in OVITO [50,52], where blue and white atoms represent bulk bcc and disordered Mo atoms, respectively. (c) A sample $\langle 100 \rangle$ -oriented bulk Mo structure with an elliptical crack (shown in the zoomed-in view).

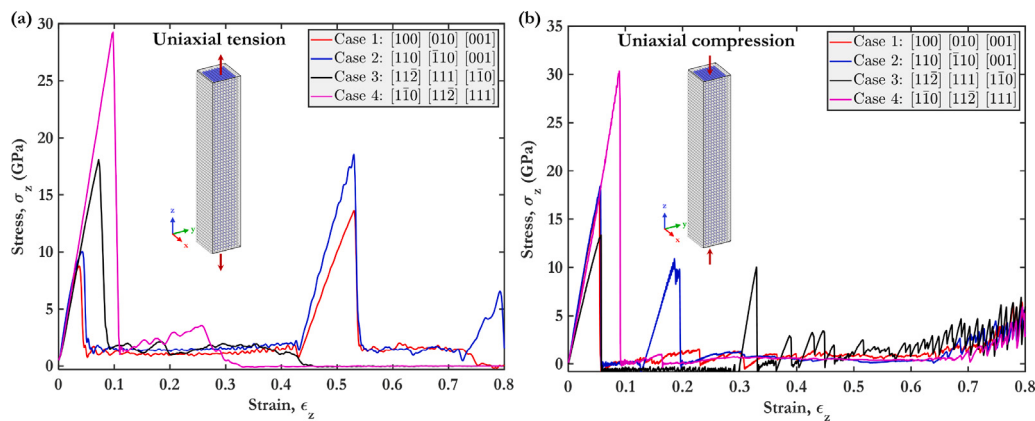


Fig. 2. Stress-strain response of all four Mo nanowire configurations under uniaxial (a) tension and (b) compression.

red and blue lines in Fig. 2a, exhibit elongated plastic deformation after yielding (high ductility), whereas in loading directions of $\langle 110 \rangle$ and $\langle 111 \rangle$, shown by black and pink lines, respectively, they exhibit limited plasticity and lean towards brittleness. The stress-strain relationships in $\langle 100 \rangle$ and $\langle 110 \rangle$ NWs align with findings reported in a previous study [45]. After the initial elastic region, cases 1 and 2 exhibit a large plastic strain region before entering the second elastic region at 40%–50% strain, with respective yield stresses of 15 GPa and 20 GPa. Despite having the same loading direction of $\langle 100 \rangle$, the two NWs have different transverse orientations, which results in a significant difference in their second yield stresses. Such a difference is explained by the atomic distribution in Section 3 of the manuscript under case 2 deformation mechanisms discussion. In contrast, while the first two structures do not completely fail until 80% strain, cases 3 and 4 fail at only 10% and 30% strain after reaching their first yield strength, respectively.

Next, Fig. 2b shows the stress-strain response of Mo NWs under uniaxial compressive loading, where cases 1, 2, and 3 show similar initial stress-strain response (yield stress \approx 15 GPa), while case 4 shows a different response to compressive loading, with yield stresses of about 30 GPa. Interestingly, case 2 and case 3, shown in solid blue and black lines in Fig. 2b, experience a second elastic region at an applied compressive strain of 10% and 30%, respectively, with a yield stress of \sim 10 GPa; this is also evident in Figs. 8 and 11, where atomistic snapshots are used to confirm second elastic regions. The second elasticity is attributed to the twin propagation and complete structural conversion into bcc_2 .

3.2. Deformation mechanisms of all NWs

Case 1 NW: $\langle 100 \rangle/\{100\}$

Fig. 3 shows atomic snapshots of case 1 Mo NW during uniaxial tensile and compressive loading conditions. Under tensile loading, after the initial yield at \sim 9 GPa, the stress decreases by around 4% strain (see red line in Fig. 2a). During this period, a small section of the fcc phase appears in the central region, with an orientation of $[110] \bar{[1}10] [001]$, as shown in Fig. 3. The fcc phase is only present for approximately 1% of the strain. As the fcc atoms disappear, $\{112\}$ twin boundaries (TBs) start to form in the vicinity of that fcc region, and a second phase of bcc_1 (bcc_1) forms and propagates subsequently. Fig. 3 clearly depicts the bcc_1 -fcc- bcc_2 transformation of case 1 NW around 4.6% of applied strain. Once the transition between fcc and bcc_2 is complete, the TBs formation is also completed and they further propagate along the NWs until all bcc_1 $\langle 100 \rangle$ re-orient into bcc_2 $\langle 110 \rangle$ phase. This re-orientation is also noted by Wang et al. [47] in their $\langle 100 \rangle/\{100\}$ structure. At 50% strain, the entirety of the structure has transformed into bcc_2 . Concurrently, the stress-strain curve (red line in Fig. 2a) indicates that the structure is beginning to yield for a second time. For uniaxial compression, fcc atoms appear at \sim 5% strain and then transform into bcc_2 at \sim 6.5% strain. The reorientation of bcc_1 atoms into bcc_2 atoms via fcc atoms is depicted by purple atoms forming from blue atoms via green atoms. This newly-formed bcc_2 sustains continued loading until \sim 18% strain when the structure undergoes sudden rupture. Note that the twinned- bcc_2 phase formed under compression does not propagate

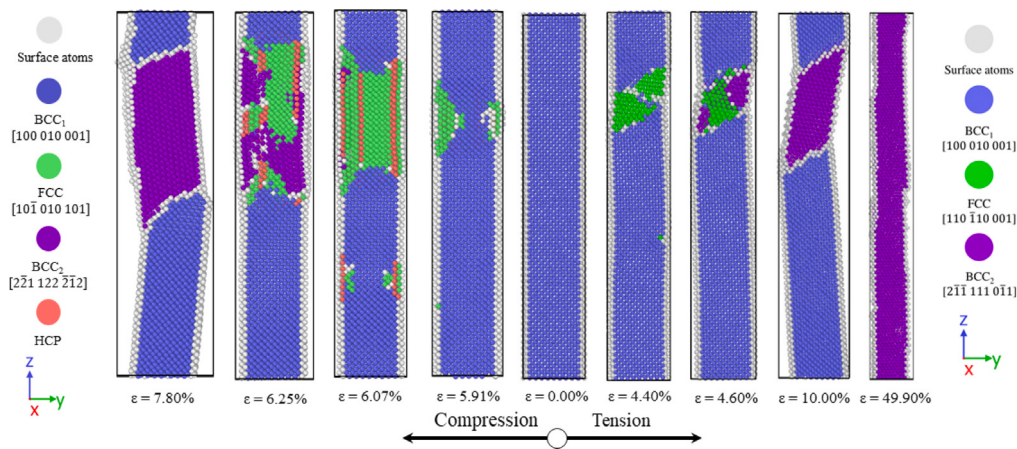


Fig. 3. Atomic snapshots of case 1 NW, with their corresponding strain values shown under each frame. All atoms are colored according to their local structure types, where blue, green, orange, purple, and white spheres represent bcc₁, fcc, hcp, bcc₂, and surface/disordered Mo atoms, respectively.

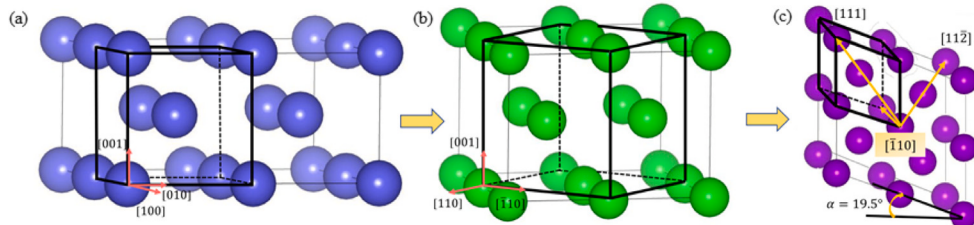


Fig. 4. Unit cell representations of (a) bcc₁, (b) fcc, and (c) bcc₂ in case 1 Mo NW under tension where frames (a)→(b) and (b)→(c) represent phase transitions via Bain and Pitsch path, respectively.

throughout the entire structure, unlike in the case of tensile loading. The twinned region begins to diminish at $\sim 7.5\%$ and continues until the structure fails at $\sim 18\%$ strain. This behavior can be attributed to the different surface features (*i.e.*, steps and roughness) present in case 1 NW compared to case 2. Further details are provided in Section 3.4 and the Supplementary document.

Although there is limited experimental evidence on phase transformations in $\langle 100 \rangle$ loaded Mo NWs, previous experimental studies have examined phase transformations in $\langle 100 \rangle$ loaded Mo nano-configurations; for example, Lu et al. [32] reported an 80 nm thinly sliced $\langle 100 \rangle$ Mo sample with a $\langle 100 \rangle$ crack undergoing a bcc-fcc (face-centered-orthorhombic) phase transition due to high-stress concentration at the crack tip, leading to a crack blunting. Another experiment showed that under vacuum conditions, MoO₃ transformed to MoO₂, with $[01\bar{1}]$ $[1\bar{1}1]$ $[211]$ and $[100]$ $[010]$ $[001]$ as the Mo orientations, respectively [63]. Although the experimental set-up and Mo-O polycrystalline structures in [63] do not align with the tensile deformation of our single-crystalline Mo NW, the relationship between the two sets of bcc orientations in Mo is consistent.

To explain the observed bcc₁-fcc-bcc₂ phase transformation, we provide a visualization of how it occurs within a unit cell using the structural schematics presented in Fig. 4. As per the definition of the Bain path, in which (001) bcc is parallel (\parallel) to (001) fcc and $[100]$ bcc \parallel $[110]$ fcc [64], it is evident that our first transformation path from bcc₁ to fcc is through Bain transformation. In other words, Fig. 4a–b show that there is no atomistic re-arrangement between bcc₁ and fcc, other than a pure tensile deformation, as the unit cell is being loaded in $\langle 100 \rangle$. Following that is the Pitsch transformation from fcc to bcc₂, shown in Fig. 4b–c, involving both tensile and rotational components [64]. If the strain is applied at an angle of 19.5° with respect to the loading direction, the fcc structure transforms from fcc to bcc₂ when viewed with $\{100\}$ as the front plane. Such transition paths have been previously reported in $\langle 100 \rangle$ -oriented thin Mo ligaments [27].

Case 2 NW: $\langle 100 \rangle/\{110\}$

The tensile stress-strain curve of case 2 NW is similar to that of case 1. The structure yields at 10 GPa and then experiences a phase transformation from bcc₁ to fcc at 5% strain, as is seen in Fig. 5. The blue line in Fig. 2a also confirms that when fcc starts to form at $\sim 5\%$ strain, the stress drops drastically. At 5.2% strain, fcc atoms disappear and then are followed by the newly transformed bcc₂ $\langle 110 \rangle$, forming $\{112\}$ TBs. Wang et al. [47] also simulated a $\langle 100 \rangle/\{110\}$ NW and observed corresponding re-orientation from bcc₁ $\langle 100 \rangle/\{110\}$ to bcc₂ $\langle 110 \rangle/\{112\}$. However, they did not identify the intermediate fcc phase that is necessary for activation of the bcc₂ phase. Once the NW is fully re-oriented to bcc₂ with a new orientation of $[100]$ $[011]$ $[\bar{0}11]$, the structure experiences a second elastic yield at 20 GPa, $\sim 1.5\times$ larger than that of case 1. The reason for this difference in behavior could be due to the difference in the secondary orientation of the NWs. In case 2, the secondary orientation is to bcc₂ $\langle 110 \rangle/\{112\}$, which may have a different mechanical properties compared to the secondary orientation in case 1 to bcc₂ $\langle 100 \rangle/\{110\}$. This highlights the importance of understanding the effect of crystallographic orientation on the mechanical properties of nanomaterials. For uniaxial compression of case 2 Mo NW, similar to that of case 1, fcc atoms appear and then transform into bcc₂, as shown in Fig. 5. After the first yielding point, contrary to case 1, bcc₂ starts growing with continued loading until $\sim 11\%$ strain, when the structure undergoes a complete transition to bcc₂ (shown by purple atoms). This is also evident from the second elastic region depicted in Fig. 2b, where the blue line has two elastic regions (bcc₁ and bcc₂).

Schematics of structural phase transformation paths of case 2 NW under tension are also visualized in Fig. 6. Interestingly, both steps of the transformation, bcc₁-fcc and fcc-bcc₂, are via the Bain path with pure tensile and no rotation included. It is worth noting that the absence of rotational deformation in case 2 NW can also be attributed to the specific orientation of the NW. The $\langle 100 \rangle$ loading direction is parallel to the $[011]$ direction of the bcc₁ phase, which is also the direction of the Bain path. This alignment in case 2 NW allows for

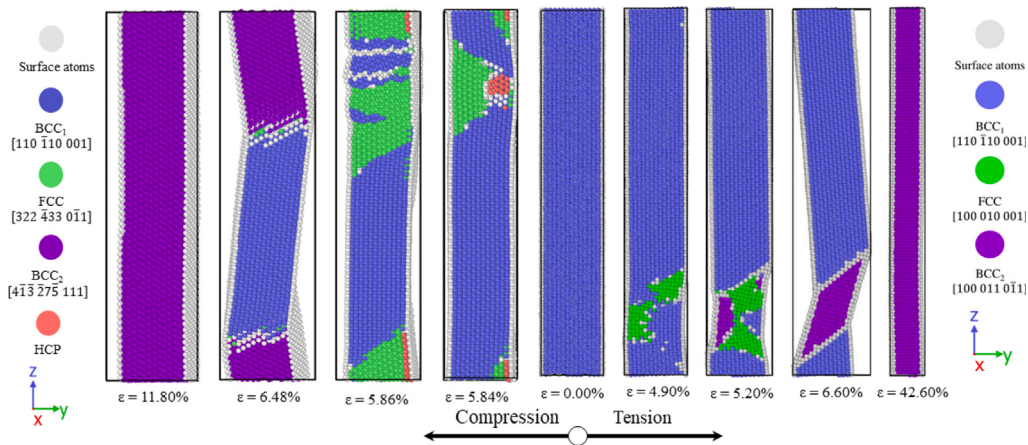


Fig. 5. Atomic snapshots of case 2 NW, with their corresponding strain values shown under each frame. All atoms are colored according to their local structure types, where blue, green, orange, purple, and white spheres represent bcc_1 , fcc, hcp, bcc_2 , and surface/disordered Mo atoms, respectively.

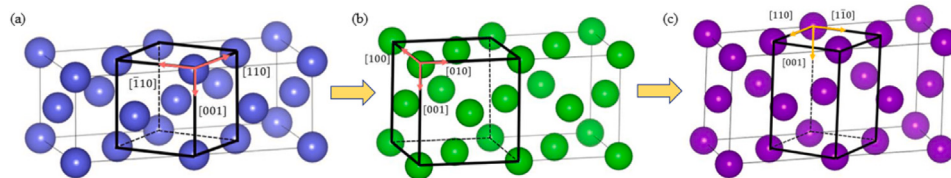


Fig. 6. Unit cell representations of (a) bcc_1 , (b) fcc, and (c) bcc_2 in case 2 Mo NW under tension where frames (a)–(b) and (b)–(c) represent phase transitions via Bain path.

uniform deformation along the Bain path without the need for rotational deformation after re-orienting to bcc_2 at 42.6% strain (Fig. 5). In comparison, case 1 NW with bcc_2 structure at 49.9% strain (Fig. 3) exhibits a rough surface with steps due to the rotational deformation of the Pitsch path. As a result, the difference in second yield stresses between case 1 and case 2 can be explained by the difference in the crystallographic orientation of the NWs. The $\langle 100 \rangle / \{110\}$ NW of case 1 has higher surface energy due to the presence of steps and rough surfaces resulting from the rotational deformation during the phase transformation. On the other hand, the $\langle 100 \rangle / \{011\}$ NW of case 2 has a lower surface energy due to the absence of rotational deformation, resulting in a smoother surface and a higher second yield stress. Based on the consistent deformation mechanism observed in both case 1 and case 2 NWs, it can be concluded that the formation of a metastable fcc phase is necessary to initiate the formation of TBs in $\langle 100 \rangle$ -loaded Mo NWs. Furthermore, it is observed that with the loading orientation of $\langle 100 \rangle$, the TBs not only form after the disappearance of fcc and the subsequent transformation to bcc_2 , but also propagate throughout the structure, leading to the reorientation of the whole NW into the bcc_2 phase.

Surface characteristics play a crucial role in influencing deformation mechanisms and resulting mechanical properties, as thoroughly discussed in a previous review article [65]. In our study, cases 1 and 2, despite having the same loading orientation (*i.e.*, [001]), exhibit different surface features, with the former having higher surface energy, as shown in Table 3, due to the presence of steps and roughness at the free surface. The impact of such surface features (*i.e.*, roughness, steps, etc.) can also be seen in Figs. 3 and 5. To elaborate, in the atomistic snapshots of Mo NW case 1 (Fig. 3), various steps and kinks are observed at the rightmost (tension) and leftmost (compression) frames. Under compression, twin propagation is hindered significantly, while under tension, twin propagates with multiple step formations at the surface, making the surface very rough. On the other hand, in case 2 (Fig. 5), the leftmost (compression) and rightmost (tension) frames show lesser roughness at the surface, facilitating easier twin propagation. Consequently, case 2 Mo NW is stronger and more ductile than case 1 due to these surface effects. Such a phenomenon is also discussed thoroughly in Section 3.4.

Case 3 NW: $\langle 110 \rangle / \{112\}$

In contrast to case 1 and 2 NWs loaded under tension, case 3 NW only undergoes limited deformation before failure, with necking occurring at 40% strain. At $\sim 7\%$ strain, fcc and hexagonal close-packed (hcp) atoms appear in alternate layers, as shown in Fig. 7, leading to a significant drop in stress according to the stress-strain curve in Fig. 2a. Subsequently, bcc_2 appears gradually at 8% strain, and at 10% strain, grain boundaries (GBs) form around the bcc_2 atoms. However, this small region of bcc_2 reverts to bcc_1 as the GBs propagate with further loading of the structure. Consequently, at the final strain of 37.9%, the entire structure returns to bcc_1 and necks to failure. Although PTM recognizes different structures in the simulation of case 3 NW, it does not necessarily indicate that phase transformation is happening. Previous studies on Mo simulations have reported no phase transformation or twinning formation in $\langle 110 \rangle$ loaded NWs or nano ligaments under tension [27, 47]. Furthermore, the fcc/hcp atoms appearing in Fig. 7 seem to occur simultaneously and form alternative layers, which have been reported as stacking fault sequences in an Au nanoribbon [66] rather than actual phase transition. However, such a Mo NW, under compressive loading, undergoes a phase transition from bcc_1 -fcc- bcc_2 , where fcc atoms tend to pave the way for the reorientation into bcc_2 atoms, as shown in the left frames of Fig. 7. This is further validated using the compressive energy curves in Section 3.3.

Case 4 NW: $\langle 111 \rangle / \{112\}$

Case 4 NW does not show any promise for bcc_1 -fcc- bcc_2 transformation. During tensile loading, case 4 Mo NW experiences a smooth transition from bcc_1 to bcc_2 . This is also evident from the computed energy plot where energy for fcc atoms reside well above the energies for bcc_1 and bcc_2 atoms. For compressive loading, such a Mo NW experiences slippage of planes first, and then some local fcc atoms appear. However, the fcc atoms do not trigger the reorientation of bcc atoms, rather similar to tensile loading, bcc_1 - bcc_2 is the primary transformation in this case. We refer the reader to the Supplementary document for further reading. Interestingly, instead of phase-transformation-mediated twin formation as observed in cases 1 and 2 under tension and 1, 2,

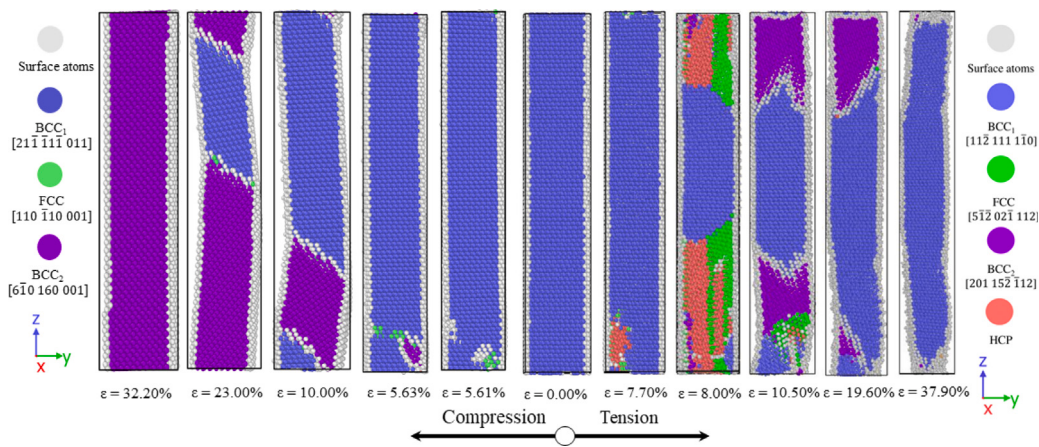


Fig. 7. Atomic snapshots of case 3 NW, with their corresponding strain values shown under each frame. All atoms are colored according to their local structure types, where blue, green, orange, purple, and white spheres represent bcc_1 , fcc, hcp, bcc_2 , and surface/disordered Mo atoms, respectively.

and 3 under compression, a more conventional twin formation (*i.e.*, deformation twin) is observed in case 4 Mo NW, as shown in Fig. 2S in the supplementary material. This twin formation is preceded by dislocation slips, as depicted in frames of Fig. 9. While it is true that this deformation mechanism itself warrants its own investigation to picture a comprehensive competition between phase-transformation-assisted twins, classical twins, and dislocation slips, it falls out of the limited scope of this study and is kept for future investigations. In addition, classical twinning does not result in uniform twin propagation throughout the structure, hence implying less significance compared to phase-transformation-assisted twin formation in terms of enhancing ductility.

3.3. Energy curve representation of phase transformation

To provide further evidence for the phase transformations, we plotted the energy-per-atom of the phases present during the deformation simulation in the NW structure using both DFT and MD calculations. Fig. 8 represents such a set of energy-per-atom plots during uniaxial tension (blue) and compression (pink), where solid and dashed lines represent MD results, while shadowed (shaded) lines represent DFT results. Frames 8a, 8b, 8c, and 8d represent energy-per-atom as a function of lattice parameters for cases 1, 2, 3, and 4, respectively. Each line represents the energy of a specific phase (*e.g.*, bcc_1 , fcc, and bcc_2) present in the NW during the deformation process; for example, in Fig. 8a, solid and shaded blue lines in the pink-shaded region are the energy-per-atom curves for bcc_2 obtained from MD and DFT, respectively. It is evident that there is a slight difference between the DFT and MD energy curves, which can be attributed to the fact that in the MD approach, only potential energy is considered, while DFT calculations account for both potential and kinetic energies. Despite this small energy gap, the two approaches are in agreement with all other aspects, such as the location of local minima and the most energetically favorable crystal structure at different strains. Note that crossing points between energy curves represent a possible change in phase during the deformation process, with the phase with lower energy preferred over the other. MD-computed energy-per-atom values slightly differ from the reference value of -6.82 eV/atom [44] due to the possible variations in phase space sampling during MD runs. Additionally, the values were slightly adjusted during the curve-fitting process, resulting in an average change of approximately 0.15% in energy values.

Fig. 8a shows the MD and DFT energy curves of case 1 Mo NW under tensile and compressive loading conditions. Solid black and white circles denote transition points computed by MD and DFT codes, respectively, except the solid black O which means the starting point

with no applied strain. For MD tension (compression) curves, the two crossing points are marked by points A (C) and B (D), where point A (C) marks the transition from bcc_1 (black) to fcc (red), and point B (D) marks the transformation from fcc (red) to bcc_2 (blue). Similarly, in DFT calculation, A' (C') and B' (D') represent the two transition points under tension (compression). The approximate coincidence of points A (C) and A' (C') demonstrates that the phase transition between bcc_1 and fcc occurs at approximately the same lattice parameter from both MD and DFT calculations. Please note that the crossing points in the energy plots coincide with the strain value at which the new phase emerges in the structure, as shown in the atomistic snapshots. Similarly, for case 2 Mo NW, it is easily seen from Fig. 8b that, in MD calculations, under uniaxial tension (compression), at crossing point A (C), bcc_1 switches to fcc, and at crossing point B (D), fcc transforms into bcc_2 . Note that crossover points obtained from MD—A, B, C, and D—coincide with those obtained from DFT—A', B', C', and D', respectively. In other words, it is fair to say that both MD and DFT agree on not only the overall energy trend but also the crossover points denoting phase transitions (*i.e.*, bcc_1 -fcc- bcc_2). Therefore, the two methods validate the observed bcc_1 -fcc- bcc_2 transformation in case 2 Mo NW. However, note that the duration of metastable fcc is slightly different under tension and compression loading, and it is also evident in the frames of Fig. 5, where fcc phase was present only up to applied strain values of $\sim 5\%$ and $\sim 6\%$ in tension and compression, respectively.

Fig. 8c represents the computed MD and DFT energy curves of case 3 Mo NW under uniaxial tensile (blue region) and compressive (pink region) loading. In the MD (DFT) calculations for tension, points A and B (A' and B') denote the crossover points between bcc_1 -fcc and fcc- bcc_2 . Point A (or A') occurs immediately before point B (or B'), which agrees with the appearance of fcc atoms for a short period of applied strain shown in the frames of Fig. 7. The energy curve therefore indicates that there is no stable phase transformation in the order of bcc_1 -fcc- bcc_2 in case 3 NW under tension. On the contrary, a crossover between solid black (bcc_1) and solid red (fcc) line is evident during compression (point C in the pink-shaded region). Such a crossover (C') is also observed from the DFT energy curves. Similarly, the fcc- bcc_2 transformation is also captured by MD and DFT calculations (depicted by points D and D', respectively). Note that, even after the formation of TB, fcc atoms appear for a large strain range near the edge of the TB, helping the TB propagate through the structure. For case 4 NW, the energy curves presented in Fig. 8d show that bcc_1 or bcc_2 remains the most stable structure (under tension) with the lowest energy. There are no intersection points between bcc_1 and fcc or between fcc and bcc_2 as fcc stays well above both bcc curves. This implies that there is no bcc_1 -fcc- bcc_2 phase transformation in case 4 NW under tension. For compression, although there are intersecting points between the

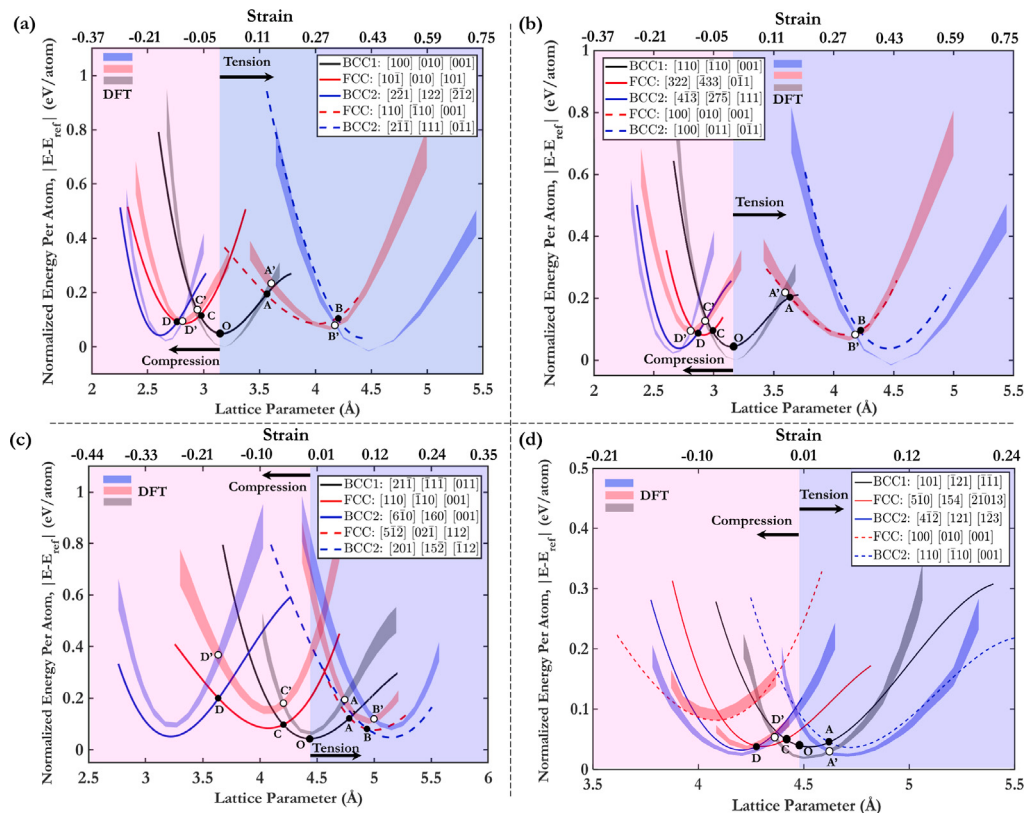


Fig. 8. Computed normalized-energy-per-atom, $|E - E_{\text{ref}}|$, as a function of lattice parameter defined as the average distance between two atomic layers during uniaxial tension and compression for (a) case 1, (b) case 2, (c) case 3, and (d) case 4 Mo NW. Corresponding strain values are shown on the top x axis of each frame where positive and negative denote tensile and compressive strain, respectively. Solid and dashed lines represent uniaxial compression and tension energy curves, respectively, while shaded (shadowed) lines represent corresponding DFT results. E_{ref} is the reference energy per atom (-6.82 eV) of Mo obtained from [44].

curves, these do not qualify for phase transformations as, for example, a few fcc atoms appear and stay near the TB but no evidence of fcc atoms changing into bcc_2 is captured during the simulations. Rather, the major deformation mechanism is recognized by slippage of $\{110\}$ planes at an applied strain of $\sim 10\%$ (Fig. 2S in the Supplementary document). This can also be verified from Fig. 2b, where the stress for case 4 NW (magenta line) drops to near-zero at a strain value of $\sim 10\%$. So, to quantify as a phase transition, both visual evidence of structural transitions (e.g., fcc atoms changing into bcc_2) and intersecting points in the energy plot from MD and DFT need to be recognized. Refer to Fig. 2S in the Supplementary document for further details. Table 2 summarizes phase transformation-assisted twin formations across all four Mo NWs for uniaxial tensile and compressive loading conditions.

Deformation mechanisms in Mo NWs can be significantly influenced by their size and diameter. Although this has yet to be thoroughly investigated for Mo NWs, the size dependence can determine whether twinning or slip is activated, potentially leading to a transition from dislocation-dominated mechanisms to twinning as the NW diameter decreases. A similar dislocation-to-twinning transition with decreasing NW diameter has been observed in a previous study on W NWs, where a quantitative analysis of the competition between dislocation slips and twins was conducted with varying NW size [67]. In another study, a similar competition between dislocations and deformation twins in W nanowires loaded along different directions is discussed thoroughly [68]. Such a competition between PT-assisted twinning, classical twinning, and dislocation slips in Mo NWs requires further investigation.

3.4. Comparison between slips and twins in NWs

The most common slip systems in bcc structures include $\{110\}$, $\{112\}$, and $\{123\}$. In our cases, during tensile deformation, $\{112\}$ twin

Table 2

Summary of phase transformations under uniaxial tension and compression across all four Mo NWs.

	Deformation	$\text{bcc}_1 \rightarrow \text{fcc}$ phase transformation	Twinning
Case 1 NW	Tension	Present	Present
	Compression	Present	Present
Case 2 NW	Tension	Present	Present
	Compression	Present	Present
Case 3 NW	Tension	Absent	Absent
	Compression	Present	Present
Case 4 NW	Tension	Absent	Present
	Compression	Absent	Present

boundaries are observed in cases 1, 2, and 4, while in case 3, a $\{110\}$ slip plane occurs, as shown in Fig. 9. During compression, cases 1, 2, and 3 experienced $\{112\}$ TBs, while a $\{110\}$ slip plane is present in case 4. To understand which slip system dominates in a structure, the Schmid factors are calculated, and the slip system with the highest Schmid factor is expected to be the dominant one [69]. From our tensile calculations (see Supplemental Material), $\{112\}$ has the highest Schmid factor for all four cases, despite the observation of $\{110\}$ slip in case 3. However, Rohith et al. [70] and Wang et al. [47] argued that surface energy also plays a significant role in determining the slip system for a structure, in addition to the Schmid factor. Therefore, we hypothesize that the surface energy of case 3 NW is lower than that of case 1, 2, and 4 under tension such that the system prefers $\{110\}$ slips over $\{112\}$ TBs. The surface energy is calculated via the equation below:

$$\gamma_s = \frac{E_s - n_s E_b}{A_s}$$

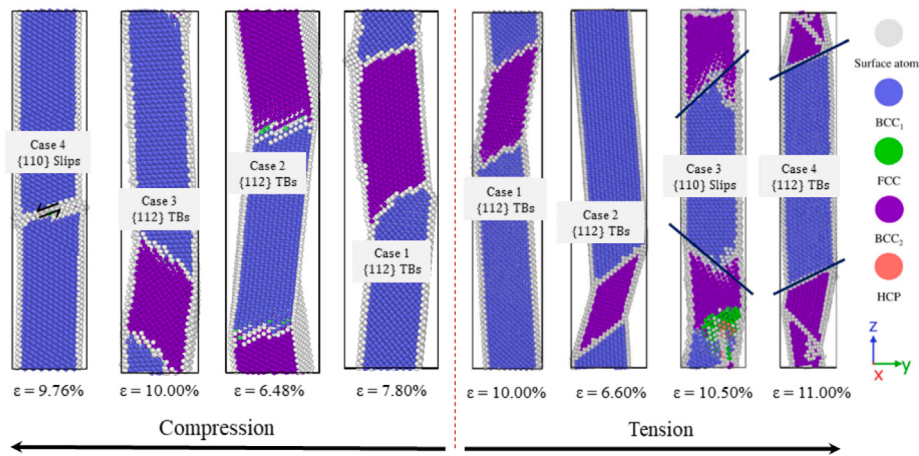


Fig. 9. Twin and slip planes in NWs during uniaxial tensile and compressive loading.

Table 3

Surface energy of all NW cases at GBs or TBs formation during tension. Surface energy is calculated when {112} TBs occur in cases 1, 2, and 4 and when {110} slip planes occur in case 3.

Tensile case no.	Surface energy, γ_s [mJ/m ²]
Case 1 NW	1802.2
Case 2 NW	1725.1
Case 3 NW	929.24
Case 4 NW	1880.0

where γ_s is the surface energy, E_s is the total energy of surface atoms, n_s is the number of surface atoms, E_b is the energy per atom of bulk atoms, and A_s is the surface area [47,71]. As a result, the surface energy of cases 1, 2, 3, and 4 at the timeframe where TBs or slips happen during tension are reported in Table 3. Here, the results agree with our hypothesis that {110} slip system is preferred over {112} TBs in case 3 NW since the surface energy is significantly lower than that in cases 1, 2, and 4 where {112} TBs occur.

Note that in case 1 compression, we observe that atoms near the bottom TB forming twinned-bcc₂ regions first move out of the {112} plane and then return to the {112} plane right before bcc₂ is formed, as shown in Fig. 4S in the Supplementary document. This rearrangement/reposition resulted from the phase transitions occurring from bcc₁ to fcc to bcc₂, recognized as phase-transformation-assisted twinning. It is worth mentioning that atomic displacements are of the nature of $a/6(111)\{112\}$ (twinning direction) across all the cases where TBs are observed, that is cases 1 and 2 under tension and cases 1, 2, and 3 under compression. Interestingly, some atoms near the rough, jagged morphology of the bottom twin boundary in case 1 compression, shown in the leftmost frame of Fig. 3, exhibit displacements of $a/6(111)\{112\}$ (twinning), while others undergo $a/3(111)\{112\}$ (anti-twinning) displacements, as depicted in Fig. 10. This suggests that the origin of such rough and stepped TBs can be correlated to a non-unique (*i.e.*, a combination of twinning and anti-twinning) shearing movement of atoms. Refer to Refs. [72,73] for detailed discussion. In addition, twinning–anti-twinning mechanisms in bcc NWs are shown to be size-dependent [72]. Future studies will focus on exploring the loading and size dependence of twinning and anti-twinning behaviors in molybdenum (Mo) materials.

3.5. Deformation mechanisms of bulk structures

To further investigate the size effects on phase transformation behavior observed in the NW simulations, bulk simulations were also conducted. For case 1, the crack tip configuration was ⟨100⟩/⟨100⟩, and for case 2, it was ⟨100⟩/⟨110⟩, with both loading directions along

⟨100⟩. These simulations were conducted to provide additional validation and insights into the phase transformation behavior observed in the NW simulations and to compare with previous experimental observations [30]. The microstructure evolution of case 1 bulk structure at various strain values is depicted in Fig. 11. The atoms follow a similar bcc₁-fcc-bcc₂ transformation sequence as observed in case 1 NW. Fig. 11a illustrates the nucleation of the fcc transient phase due to high-stress concentration at the crack tip. As the tensile strain increases, the density of fcc phase atoms also grows proportionally. Between 4.9% and 6.8% strain, the fcc region moves across the crack. At the end of the movement, as fcc atoms start to disappear, the newly oriented bcc₂ atoms follow, and {112}/⟨111⟩ TBs form around the bcc₂ region. The crystallographic orientations of these two phases, fcc, and bcc₂, are consistent with the ones observed in case 1 NW, which follows a Pitsch path transformation (Fig. 4b-c). With further loading, the regions with TBs grow larger as the TBs propagate in the loading direction along the y-axis. Interestingly, the orientations of all phases recognized from this bulk structure are identical to the ones from case 1 NW. This implies that the bcc-fcc-bcc phase transformation also follows the Bain and Pitsch paths for bulk structures similar to the NWs.

Wang et al. [30] observed similar behavior in both their experiment and simulation results on a bulk structure with a ⟨100⟩ crack tip. In their simulation, as tensile stress is being applied along a similar direction to our case 1 bulk structure (Fig. 11), fcc atoms originate from the crack tip and expand as branches into the original bcc structure. Once the boundaries between the new fcc and the original bcc atoms are formed, new bcc structures (bcc₂) grow following the disappearance of the fcc atoms. Wang et al.'s [30] experimental TEM results also suggest that fcc and bcc₂ are two distinct phases but not distorted versions of each other. Therefore, the fcc phase is indeed a metastable state to initiate the twin boundary formation and the reorientation of the bcc₁ to bcc₂ phase. This bcc₁-fcc-bcc₂ sequence of phase transformation is identical to the sequence observed in our simulation as well as in their experimental TEM results. However, the authors [30] suggested that the phase transitions in their work followed the Nishiyama–Wassermann (N–W) and Kurdjumov–Sachs (K–S) paths instead of Bain and Pitsch paths as in our NW and bulk simulations. In addition, it is detected from our simulation that the boundaries between bcc₂ and bcc₁ atoms are TBs due to the symmetrical geometry of ⟨001⟩ bcc₁ and ⟨110⟩ bcc₂. In Wang et al.'s experiment and simulation [30], ⟨001⟩ bcc₁ and ⟨111⟩ bcc₂ were reported instead, and no TBs observation was proposed.

It can be concluded from the consistency of all present phases between case 1 NW and bulk structure that the fcc phase is a necessary transient phase that sets up TBs for formation and propagation, leading to the reorientation of bcc structures. Another bulk configuration, case 2 of ⟨100⟩/⟨110⟩, is also simulated, providing similar results and conclusions as in case 1 (see Fig. 3S in Supplemental Material).

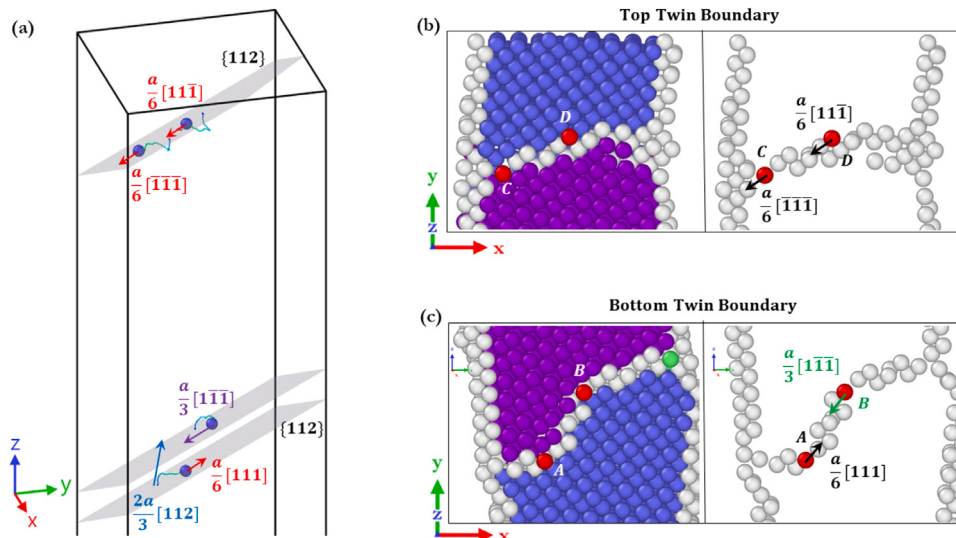


Fig. 10. (a) Atomistic snapshots of case 1 Mo NW under compression ($\epsilon_z = 7.50\%$) showing how individual BCC_1 atoms (blue spheres) transform into disordered (white, twin boundary) atoms, with their corresponding shearing directions shown. Frames (b) and (c) represent atomic snapshots of displacement vectors of two representative atoms (each) at the top and bottom TBs, respectively. Atoms A and B represent two such atoms at the bottom TB, while atoms C and D denote top TB representative atoms. Here, $a/6\langle 111 \rangle \{112\}$ = twinning, $a/3\langle 111 \rangle \{112\}$ = anti-twinning, $2a/3\langle 112 \rangle$ = PT-driven out-of-plane displacement.

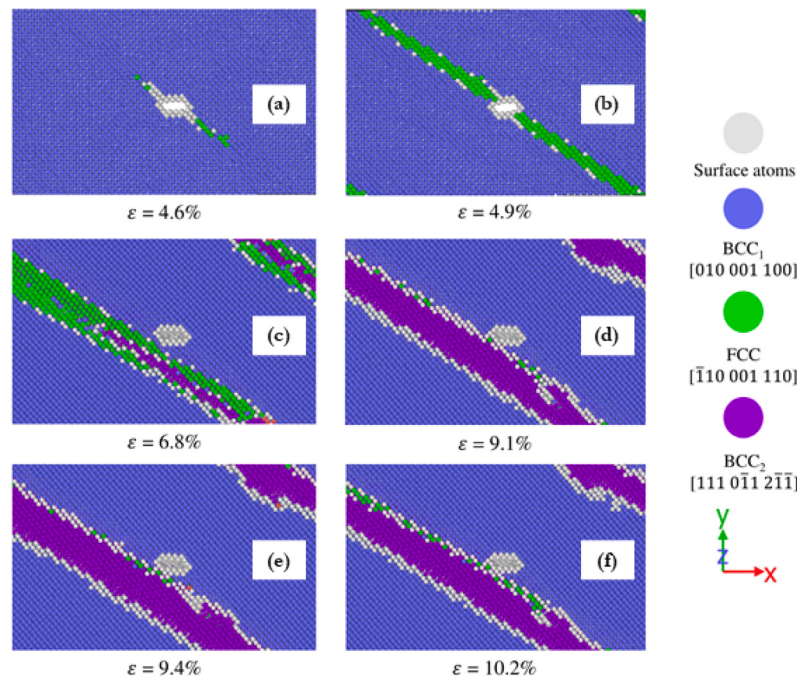


Fig. 11. Atomistic snapshots of case 1 bulk Mo with an elliptical crack (loaded along y direction). Frames (a) to (f) represent the response of the structure with increasing applied strain (shown under each frame). All atoms are colored according to their local structure types, where blue, green, purple, and white spheres represent BCC_1 , fcc, BCC_2 , and disordered Mo atoms, respectively.

4. Conclusion

In summary, we have examined the effects of crystallographic orientation on the deformation mechanisms — twins or slips — in Mo nanowires and bulk structures with cracks under uniaxial loading (tensile and compressive) conditions using atomistic simulations. Our study reveals that the phase-transformation-assisted twinning phenomenon is a promising pathway to developing stronger and more ductile nanoscale materials, promising new frontiers of advanced materials design.

In this study, we report on the deformation mechanisms in four differently oriented Mo NWs. Notably, the role of the metastable fcc

state in the BCC_1 -fcc- BCC_2 transformation, followed by $\{112\}$ twin formation and propagation, is evident in $\langle 100 \rangle$ -loaded NWs under both tension and compression. This observed $\{112\}$ twin plane formation was prefaced by a metastable fcc phase that transitioned from the initial bcc phase in response to applied deformation. It is noted that highly localized stress concentrations originating from NW surfaces aided in the phase-transformation-assisted twinning mechanisms. A similar behavior was also observed near local high-stress regions at the tip of a crack in bulk Mo structures, bolstering the hypothesis that the orientation-dependent deformation mechanism in Mo can be achieved across multi-dimensional Mo structures (*i.e.*, 1D for NWs and 3D for

bulk Mo). Our study then goes into the in-depth analysis of the evidence of such a phase-transformation-assisted twinning phenomenon in {100}-loaded bulk Mo, elucidating the role of high-stress concentration regions in phase transformation and twin formation.

Next, {110}-loaded NWs exhibit the formation of an intermediate fcc phase before the formation of {112} twin boundaries, but only under compression. The tensile counterpart of {110}-loaded Mo deforms primarily by activating {110} slip system. Interestingly, {111}-loaded NWs do not show any potential for phase-transformation-assisted twinning, failing solely by activating {110} or {112} slip systems. The orientation relationships (e.g., Bain or Pitsch) between the initial and transformed phases are also discussed in detail, explaining the pathway of phase transitions (i.e., bcc₁→fcc or fcc→bcc₂).

Our findings of metastable fcc state and subsequent reoriented bcc phases are further corroborated by DFT and MD energy calculations. By deforming unit cells and recording the energy of each deformed state, we identify the lowest energy state for any given deformation, providing robust evidence for the metastable fcc state being more favorable than the bcc state under certain conditions. Understanding the phase transformation mechanisms and their role in subsequent twin boundary formation in Mo NWs is a major step towards developing ductile yet stronger one-dimensional and bulk Mo-based nanomaterials. Therefore, this study provides valuable insights into orientation-dependent phase transitions of bcc materials, and these insights can be leveraged and used as a guide to design materials or alloys with enhanced mechanical properties for advanced applications, including flexible electronics, high-strength composites, and nanoscale devices [74,75].

CRediT authorship contribution statement

Afnan Mostafa: Writing – review & editing, Writing – original draft, Visualization, Validation, Software, Methodology, Investigation, Data curation. **Linh Vu:** Writing – original draft, Visualization, Validation, Software, Methodology, Investigation, Data curation, Conceptualization. **Zheming Guo:** Writing – original draft, Visualization, Validation, Methodology, Formal analysis, Data curation, Conceptualization. **Ali K. Sharq:** Writing – review & editing. **Aditya Dey:** Writing – review & editing, Writing – original draft, Validation, Software, Methodology, Data curation. **Hesam Askari:** Writing – review & editing, Validation, Supervision, Project administration, Investigation, Conceptualization. **Niaz Abdolrahim:** Writing – review & editing, Writing – original draft, Visualization, Validation, Supervision, Software, Resources, Project administration, Methodology, Investigation, Funding acquisition, Formal analysis, Data curation, Conceptualization.

Declaration of competing interest

The authors declare that they have no known competing financial interests or personal relationships that could have appeared to influence the work reported in this paper.

Data availability

The data supporting the findings of this study are available from the corresponding author upon reasonable request.

Acknowledgments

This material is based upon work supported by the National Science Foundation, United States under Grant No. 2208681. We also acknowledge the support of the 2022 Discover Grant (Schwartz Undergraduate Research Fund) and the Center for Integrated Research Computing at the University of Rochester. We also appreciate the insights from Dr. Eugen Rabkin, Dr. Anuj Bisht from Technion – the Israel Institute of Technology, and the Advanced Computational Mechanics and Materials Laboratory at the University of Rochester.

Appendix A. Supplementary data

Supplementary material related to this article can be found online at <https://doi.org/10.1016/j.commatsci.2024.113273>.

References

- [1] S. Dudarev, J.-L. Boutard, R. Lässer, M. Caturla, P. Derlet, M. Fivel, C.-C. Fu, M.Y. Lavrentiev, L. Malerba, M. Mrovec, et al., The EU programme for modelling radiation effects in fusion reactor materials: An overview of recent advances and future goals, *J. Nucl. Mater.* 386 (2009) 1–7.
- [2] S. Zinkle, N. Ghoniem, Operating temperature windows for fusion reactor structural materials, *Fusion Eng. Des.* 51 (2000) 55–71.
- [3] A.E. Sand, J. Byggmästar, A. Zitting, K. Nordlund, Defect structures and statistics in overlapping cascade damage in fusion-relevant bcc metals, *J. Nucl. Mater.* 511 (2018) 64–74.
- [4] G.-Q. Yan, X.-L. Cheng, H. Zhang, Z.-Y. Zhu, D.-H. Ren, Different effects of electronic excitation on metals and semiconductors, *Phys. Rev. B* 93 (21) (2016) 214302.
- [5] T.K. Yamada, L. Gerhard, T. Balashov, A.F. Takács, R.J. Wesselink, W. Wulfhekel, Electric field control of fe nano magnets: towards metallic nonvolatile data storage devices, *Japan. J. Appl. Phys.* 50 (8S3) (2011) 08LA03.
- [6] D.-S. Xu, J.-P. Chang, J. Li, R. Yang, D. Li, S. Yip, Dislocation slip or deformation twinning: confining pressure makes a difference, *Mater. Sci. Eng. A* 387 (2004) 840–844.
- [7] S. Ogata, J. Li, S. Yip, Energy landscape of deformation twinning in bcc and fcc metals, *Phys. Rev. B* 71 (22) (2005) 224102.
- [8] C. Chisholm, H. Bei, M. Lowry, J. Oh, S.S. Asif, O. Warren, Z. Shan, E.P. George, A.M. Minor, Dislocation starvation and exhaustion hardening in Mo alloy nanofibers, *Acta Mater.* 60 (5) (2012) 2258–2264.
- [9] J.-Y. Kim, D. Jang, J.R. Greer, Tensile and compressive behavior of tungsten, molybdenum, tantalum and niobium at the nanoscale, *Acta Mater.* 58 (7) (2010) 2355–2363.
- [10] L. Huang, Q.-J. Li, Z.-W. Shan, J. Li, J. Sun, E. Ma, A new regime for mechanical annealing and strong sample-size strengthening in body centred cubic molybdenum, *Nature Commun.* 2 (1) (2011) 547.
- [11] D. Caillard, Kinetics of dislocations in pure Fe. Part I. In situ straining experiments at room temperature, *Acta Mater.* 58 (9) (2010) 3493–3503.
- [12] J.-Y. Kim, D. Jang, J.R. Greer, Crystallographic orientation and size dependence of tension-compression asymmetry in molybdenum nano-pillars, *Int. J. Plast.* 28 (1) (2012) 46–52.
- [13] L. Lu, X. Chen, X. Huang, K. Lu, Revealing the maximum strength in nanotwinned copper, *Science* 323 (5914) (2009) 607–610.
- [14] K. Kumar, H. Van Swygenhoven, S. Suresh, Mechanical behavior of nanocrystalline metals and alloys, *Acta Mater.* 51 (19) (2003) 5743–5774.
- [15] L. He, N. Abdolrahim, Mechanical enhancement of graded nanoporous structure, *J. Eng. Technol.* 144 (1) (2022) 011007.
- [16] N. Abdolrahim, I. Mastorakos, H.M. Zbib, Deformation mechanisms and pseudoelastic behaviors in trilayer composite metal nanowires, *Phys. Rev. B* 81 (5) (2010) 054117.
- [17] L. He, N. Abdolrahim, Deformation mechanisms and ductility enhancement in core-shell Cu@Ni nanoporous metals, *Comput. Mater. Sci.* 150 (2018) 397–404.
- [18] X. Wang, J. Wang, Y. He, C. Wang, L. Zhong, S.X. Mao, Unstable twin in body-centered cubic tungsten nanocrystals, *Nature Commun.* 11 (1) (2020) 2497.
- [19] G. Yang, S.-J. Park, Deformation of single crystals, polycrystalline materials, and thin films: A review, *Materials* 12 (12) (2019) 2003.
- [20] Q. Wang, J. Wang, J. Li, Z. Zhang, S.X. Mao, Consecutive crystallographic reorientations and superplasticity in body-centered cubic niobium nanowires, *Sci. Adv.* 4 (7) (2018) 8850.
- [21] H. Liu, A.K. Sharq, N. Abdolrahim, Mining structure-property linkage in nanoporous materials using an interpretative deep learning approach, *Materialia* 21 (2022) 101275.
- [22] H. Liu, L. He, N. Abdolrahim, Molecular dynamics simulation studies on mechanical properties of standalone ligaments and networking nodes, a connection to nanoporous material, *Modelling Simul. Mater. Sci. Eng.* 26 (7) (2018) 075001.
- [23] L. He, M. Hadi, H. Liu, N. Abdolrahim, Mechanism of coarsening and deformation behavior of nanoporous Cu with varying relative density, *J. Mater. Res.* 35 (19) (2020) 2620–2628.
- [24] H. Liu, N. Abdolrahim, A modified scaling law for stiffness of nanoporous materials based on gyroid cell model, *Int. J. Mech. Sci.* 166 (2020) 105223.
- [25] N. Abdolrahim, I. Mastorakos, S. Shao, D. Bahr, H. Zbib, The effect of interfacial imperfections on plastic deformation in nanoscale metallic multilayer composites, *Comput. Mater. Sci.* 86 (2014) 118–123.
- [26] X. Li, Q. Zhao, Y. Tian, Q. Wang, J. Fan, K. Song, H. Zhou, J. Wang, Phase transformation induced transitional twin boundary in body-centered cubic metals, *Acta Mater.* 249 (2023) 118815.
- [27] L. He, N. Abdolrahim, Stress-assisted structural phase transformation enhances ductility in Mo/Cu bicontinuous intertwined composites, *ACS Appl. Nano Mater.* 2 (4) (2019) 1890–1897.

- [28] S. Chu, F. Zhang, D. Chen, M. Chen, P. Liu, Atomic-scale in situ observations of reversible phase transformation assisted twinning in a CrCoNi medium-entropy alloy, *Nano Lett.* (2024).
- [29] P. Yu, R. Feng, J. Du, S. Shinzato, J.-P. Chou, B. Chen, Y.-C. Lo, P.K. Liaw, S. Ogata, A. Hu, Phase transformation assisted twinning in a face-centered-cubic FeCrNiCoAl_{0.36} high entropy alloy, *Acta Mater.* 181 (2019) 491–500.
- [30] S. Wang, H. Wang, K. Du, W. Zhang, M. Sui, S. Mao, Deformation-induced structural transition in body-centred cubic molybdenum, *Nature Commun.* 5 (1) (2014) 3433.
- [31] Y. Lu, S. Xiang, L. Xiao, L. Wang, Q. Deng, Z. Zhang, X. Han, Dislocation “bubble-like-effect” and the ambient temperature super-plastic elongation of body-centred cubic single crystalline molybdenum, *Sci. Rep.* 6 (1) (2016) 22937.
- [32] Y. Lu, S. Sun, Y. Zeng, Q. Deng, Y. Chen, Y. Li, X. Li, L. Wang, X. Han, Atomistic mechanism of nucleation and growth of a face-centered orthogonal phase in small-sized single-crystalline Mo, *Mater. Res. Lett.* 8 (9) (2020) 348–355.
- [33] A. Kedarnath, R. Kapoor, A. Sarkar, Classical molecular dynamics simulations of the deformation of metals under uniaxial monotonic loading: A review, *Comput. Struct.* 254 (2021) 106614.
- [34] R. Komanduri, N. Chandrasekaran, L. Raff, Molecular dynamics (MD) simulation of uniaxial tension of some single-crystal cubic metals at nanolevel, *Int. J. Mech. Sci.* 43 (10) (2001) 2237–2260.
- [35] N. Abdolrahim, H.M. Zbib, D.F. Bahr, Multiscale modeling and simulation of deformation in nanoscale metallic multilayer systems, *Int. J. Plast.* 52 (2014) 33–50.
- [36] A. Mostafa, A. Weerasinghe, A. Ramasubramaniam, D. Maroudas, Response of interlayer-bonded bilayer graphene to shear deformation, *J. Appl. Phys.* 134 (15) (2023).
- [37] A.K. Shargh, G.R. Madejski, J.L. McGrath, N. Abdolrahim, Molecular dynamics simulations of brittle to ductile transition in failure mechanism of silicon nitride nanoporous membranes, *Mater. Today Commun.* 25 (2020) 101657.
- [38] A.K. Shargh, G.R. Madejski, J.L. McGrath, N. Abdolrahim, Mechanical properties and deformation mechanisms of amorphous nanoporous silicon nitride membranes via combined atomistic simulations and experiments, *Acta Mater.* 222 (2022) 117451.
- [39] A. Mostafa, A. Ramasubramaniam, D. Maroudas, Thermal conductivity of 2D diamond superstructures in interlayer-bonded twisted bilayer graphene, *Appl. Phys. Lett.* 122 (13) (2023).
- [40] A. Mostafa, M. Motalab, A.R. Faiyaz, R. Paul, Uniaxial and cyclic stress-strain behavior of lead-free solders at nanoscale, in: AIP Conf. Proc., vol. 2324, AIP Publishing, 2021.
- [41] J. Wang, R.G. Hoagland, A. Misra, Phase transition and dislocation nucleation in Cu-Nb layered composites during physical vapor deposition, *J. Mater. Res.* 23 (2008) 1009–1014.
- [42] Z. Jian, Y. Chen, S. Xiao, L. Wang, X. Li, K. Wang, H. Deng, W. Hu, Molecular dynamic simulations of plasticity and phase transition in Mg polycrystalline under shock compression, *Appl. Phys. Express* 15 (1) (2022) 015503.
- [43] B.P. Sahu, C.C. Walker, G. Pharr, A. Misra, Nanoscale phase transition in impact indented Mo/Cu thin films, *Scr. Mater.* 240 (2024) 115846.
- [44] H. Gong, L. Kong, B. Liu, Metastability of an immiscible Cu-Mo system calculated from first-principles and a derived n-body potential, *Phys. Rev. B* 69 (2) (2004) 024202.
- [45] J. Wang, W. Hu, X. Li, S. Xiao, H. Deng, Strain-driven phase transition of molybdenum nanowire under uniaxial tensile strain, *Comput. Mater. Sci.* 50 (2) (2010) 373–377.
- [46] W. Hu, X. Shu, B. Zhang, Point-defect properties in body-centered cubic transition metals with analytic EAM interatomic potentials, *Comput. Mater. Sci.* 23 (1–4) (2002) 175–189.
- [47] P. Wang, W. Chou, A. Nie, Y. Huang, H. Yao, H. Wang, Molecular dynamics simulation on deformation mechanisms in body-centered-cubic molybdenum nanowires, *J. Appl. Phys.* 110 (9) (2011).
- [48] G. Ackland, R. Thetford, An improved N-body semi-empirical model for body-centred cubic transition metals, *Phil. Mag. A* 56 (1) (1987) 15–30.
- [49] A.P. Thompson, H.M. Aktulga, R. Berger, D.S. Bolintineanu, W.M. Brown, P.S. Crozier, P.J. in't Veld, A. Kohlmeyer, S.G. Moore, T.D. Nguyen, et al., LAMMPS—a flexible simulation tool for particle-based materials modeling at the atomic, meso, and continuum scales, *Comput. Phys. Comm.* 271 (2022) 108171.
- [50] A. Stukowski, Visualization and analysis of atomistic simulation data with OVITO—the open visualization tool, *Modelling Simul. Mater. Sci. Eng.* 18 (1) (2009) 015012.
- [51] D. Faken, H. Jónsson, Systematic analysis of local atomic structure combined with 3D computer graphics, *Comput. Mater. Sci.* 2 (2) (1994) 279–286.
- [52] P.M. Larsen, S. Schmidt, J. Schiotz, Robust structural identification via polyhedral template matching, *Modelling Simul. Mater. Sci. Eng.* 24 (5) (2016) 055007.
- [53] L. Zhao, X. Song, C. Gong, D. Zhang, R. Wang, R.N. Zare, X. Zhang, Sprayed water microdroplets containing dissolved pyridine spontaneously generate pyridyl anions, *Proc. Natl. Acad. Sci.* 119 (12) (2022) e2200991119.
- [54] S. Smidstrup, T. Markussen, P. Vancraeyveld, J. Wellendorff, J. Schneider, T. Gunst, B. Verstichel, D. Stradi, P.A. Khomyakov, U.G. Vej-Hansen, et al., QuantumATK—an integrated platform of electronic and atomic-scale modelling tools, *J. Condens. Matter Phys.* 32 (1) (2019) 015901.
- [55] A. Dey, A. Azizimanesh, S.M. Wu, H. Askari, Uniaxial strain-induced stacking order change in trilayer graphene, *ACS Appl. Mater. Interfaces* 16 (6) (2024) 8169–8183.
- [56] A. Dey, S.A. Chowdhury, T. Peña, S. Singh, S.M. Wu, H. Askari, An atomistic insight into Moiré reconstruction in twisted bilayer graphene beyond the magic angle, *ACS Appl. Eng. Mater.* 1 (3) (2023) 970–982.
- [57] T. Peña, A. Dey, S.A. Chowdhury, A. Azizimanesh, W. Hou, A. Sewaket, C. Watson, H. Askari, S.M. Wu, Moiré engineering in 2D heterostructures with process-induced strain, *Appl. Phys. Lett.* 122 (14) (2023).
- [58] W. Hou, A. Azizimanesh, A. Dey, Y. Yang, W. Wang, C. Shao, H. Wu, H. Askari, S. Singh, S.M. Wu, Strain engineering of vertical molybdenum ditelluride phase-change memristors, *Nat. Electron.* 7 (1) (2024) 8–16.
- [59] P. Kumar, A. Dey, J. Roques, L. Assaud, S. Franger, P. Parida, V. Biju, Photoexfoliation synthesis of 2D materials, *ACS Mater. Lett.* 4 (2) (2022) 263–270.
- [60] A. Azizimanesh, A. Dey, S.A. Chowdhury, E. Wenner, W. Hou, T. Peña, H. Askari, S.M. Wu, Strain engineering in 2D hBN and graphene with evaporated thin film stressors, *Appl. Phys. Lett.* 123 (4) (2023).
- [61] G. Kresse, J. Furthmüller, Efficient iterative schemes for ab initio total-energy calculations using a plane-wave basis set, *Phys. Rev. B* 54 (16) (1996) 11169.
- [62] A. Dey, B.A. Baraiya, S. Adhikary, P.K. Jha, First-principles calculations of the effects of edge functionalization and size on the band gap of Be₃N₂ nanoribbons: Implications for nanoelectronic devices, *ACS Appl. Nano Mater.* 4 (1) (2020) 493–502.
- [63] J. Chen, Q. Wei, Phase transformation of molybdenum trioxide to molybdenum dioxide: An in-situ transmission electron microscopy investigation, *Int. J. Appl. Ceram. Technol.* 14 (5) (2017) 1020–1025.
- [64] C. Cayron, One-step model of the face-centred-cubic to body-centred-cubic martensitic transformation, *Acta Crystallogr. A* 69 (5) (2013) 498–509.
- [65] X. Li, Z. Zhang, J. Wang, Deformation twinning in body-centered cubic metals and alloys, *Prog. Mater. Sci.* (2023) 101160.
- [66] A. Kismarahardja, Z. Wang, D. Li, L. Wang, L. Fu, Y. Chen, Z. Fan, Y. Chen, X. Han, H. Zhang, et al., Deformation-induced phase transformations in gold nanoribbons with the 4H phase, *ACS Nano* 16 (2) (2022) 3272–3279.
- [67] J. Wang, A.H. Faisal, X. Li, Y. Hong, Q. Zhu, H. Bei, Z. Zhang, S.X. Mao, C.R. Weinberger, Discrete twinning dynamics and size-dependent dislocation-to twin transition in body-centred cubic tungsten, *J. Mater. Sci. Tech.* 106 (2022) 33–40.
- [68] J. Wang, Z. Zeng, C.R. Weinberger, Z. Zhang, T. Zhu, S.X. Mao, In situ atomic-scale observation of twinning-dominated deformation in nanoscale body-centred cubic tungsten, *Nature Mater.* 14 (6) (2015) 594–600.
- [69] W. Abuzaid, H. Sehitoglu, Critical resolved shear stress for slip and twin nucleation in single crystalline FeNiCoCrMn high entropy alloy, *Mater. Charact.* 129 (2017) 288–299.
- [70] P. Rohith, G. Sainath, B. Choudhary, Double reorientation in {110} Cu nanowires, *Phil. Mag. Lett.* 97 (10) (2017) 408–416.
- [71] J. Che, C.T. Chan, W. Jian, T.-C. Leung, Surface atomic structures, surface energies, and equilibrium crystal shape of molybdenum, *Phys. Rev. B* 57 (3) (1998) 1875.
- [72] J. Wang, Z. Zeng, M. Wen, Q. Wang, D. Chen, Y. Zhang, P. Wang, H. Wang, Z. Zhang, S.X. Mao, et al., Anti-twinning in nanoscale tungsten, *Sci. Adv.* 6 (23) (2020) eaay2792.
- [73] R. Gröger, J. Holzer, T. Kruml, Twinning and antitwinning in body-centered cubic metals, *Comput. Mater. Sci.* 216 (2023) 111874.
- [74] J. Yeom, G. Lorenzini, C. Cancellieri, J. Janczak-Rusch, Evaluation of residual stresses in Cu/Mo, Cu/Nb nanomultilayers with a strong fiber texture, *Matter. Lett.* 352 (2023) 135074.
- [75] J. Yeom, G. Lorenzini, L. Ghisalberti, C. Cancellieri, J. Janczak-Rusch, The thermal stability and degradation mechanism of Cu/Mo nanomultilayers, *Sci. Technol. Adv. Mater.* 25 (2024) 2357536, just-accepted.